Geodetic Coupling Models as Constraints on Stochastic Earthquake Ruptures: An Example Application to PTHA in Cascadia

David T. Small[1] & Diego Melgar[1]

[1]Department of Earth Sciences, University of Oregon, Eugene OR, USA

Abstract

Current stochastic rupture modeling techniques do not consider the influence of first order fault zone characteristics. One such key characteristic is fault slip deficit or inter-seismic locking which has shown correlation between areas of high coupling and areas of greater slip in many recent large ruptures globally. Therefore, it is reasonable to assume that it should be considered as prior information in rupture modeling. Here, we first present a mathematical formalism to introduce locking models as prior information into stochastic rupture modeling. We then focus on how introducing slip deficit information into the stochastic rupture models influences slip distributions for the Cascadia Subduction Zone (CSZ). We compare rupture models created with two end member models of locking, one with a fully locked zone extending to the trench and another with locking deeper downdip, along with models created without a prior knowledge of locking. Large variations occur and correlate well with areas with the largest differences in slip deficit. To exemplify their impacts, the ruptures are then used for probabilistic tsunami hazard assessment. We find that overall the tsunami amplitudes generated are much more hazardous in the northern extent of the CSZ where differences in locking distribution are more prevalent. Although large uncertainties are present in accuracy of locking, imposing either constraint created very different hazard estimations when compared to the hazards where no prior locking information was used. This highlights the necessity to expand seafloor instrumentation and to consider first order fault information like locking in future authoritative hazard assessments.

1. Introduction

Using stochastic slip ruptures has become an increasingly popular tool for modeling potential future large earthquakes. Fundamentally, stochastic modeling revolves around the assumption that the distribution of coseismic slip on a fault can be considered a spatially random field (Mai & Beroza, 2002). In particular, for regions where large earthquakes are likely and where observations are limited, a substantial number of source models can be formulated if one can reasonably assume the statistical parameters (the correlation function) of the random field. Then, for a given magnitude of interest, we can generate any number of slip distributions by making random draws from the appropriate distribution. This approach has been found quite useful in a number of hazards related applications. For instance, the stochastic ruptures can be used to generate strong motion seismograms to study the potential ground motions in a specific region of interest (e.g. Graves et al., 2011, Frankel et al., 2018). The time-histories from these stochastic sources can even be used for analyzing the response of structures and critical infrastructure to potential future earthquakes (Bijelic et al., 2018). Likewise, stochastic sources and their resulting seismic and geodetic waveforms can be used to test the response of earthquake early warning systems (Ruhl et al., 2017, Goldberg & Melgar, 2020) and tsunami early warning systems that rely on onshore data (Williamson et al., 2020). This same approach is now becoming common practice in probabilistic tsunami hazard analysis (PTHA) where stochastic source modeling, when connected with advanced numerical models that simulate tsunami propagation, are also rapidly becoming a mainstay of that field (Grezio et al. 2017).

Like the advances in stochastic source modeling, tectonic geodesy has also progressed substantially. For example, it has become commonplace to use measurements of the long-term inter-seismic velocity field to identify which portions of faults are more or less locked. A review of this can be found in Bock & Melgar, 2016. Although our ability to predict future earthquakes is limited, we are able to relate these locking, or coupling models, to long-term future earthquake potentials. Notably in the robust California earthquake hazard model UCERF3 (Field et al., 2017) the inter-seismic surface velocity field is used to constrain long term “slip rates” of faults which are a primary constraint to determine the moment budget over broad areas along a fault zone. Overall, it is generally agreed that where locking is higher and faults are accumulating a slip deficit at a faster rate, earthquakes are more likely to occur. Similarly, the areas with the greatest amount of slip during large ruptures often correlate with highly locked patches of the fault zone. This relationship between locking and slip is seen in previous large ruptures across a range of fault zones including Sumatra, Japan, South America, and Alaska (e.g. Konca et al., 2005; Ozawa et al., 2011; Li and Freymueller, 2018; Moreno et al., 2010; Barnhard et al., 2016).

This correlation is not perfect, however, and the present-day pattern of heterogeneous locking on a fault does not equate to the pattern of slip during the next earthquake. There are a myriad of other controlling variables such as the complex fault geometries, past and present stress regimes, and rupture dynamics to name a few, which can be unique to each fault zone. This creates large uncertainty in how a future earthquake will rupture. In spite of these, it remains true that highly locked fault patches are accumulating a slip deficit at a faster rate and thus have a larger budget of available slip to use during the next event. Here we will show how to use that fault locking to condition the likelihood of where slip should be expected in future earthquakes. Our proposed approach does not require, in a deterministic sense, that high slip occur in highly locked patches, rather it increases the probability that it does. As a result, over many stochastic rupture simulations, on average, more slip will occur where inter-seismic locking is higher and less where locking is lower. However, for any one particular realization, slip can still be high in a low coupling region, and low in a highly locked region.

To illustrate the impact of this we will show how assuming different locking models impacts PTHA in the Cascadia Subduction Zone (CSZ) in particular. We focus specifically on the tsunami hazards because subsequent to the 2004 **M**9.2 Sumatra earthquake and tsunami which led to 240,000 casualties, probabilistic tsunami hazard assessment (PTHA, Geist & Parsons, 2006; Grezio et al., 2017) has become a rapidly expanding methodology used for assessing the hazard potential of future earthquakes and tsunamis. Unlike site-specific tsunami studies, PTHA is rooted in determination of the probability of exceeding some threshold of tsunami intensity measure (e.g. tsunami arrival height) for one or many target sites for a given return period (e.g. 100 years). A fundamental difficulty addressed by application of PTHA is that awareness of previous historical tsunamis past hundreds to thousands of years is limited and sometimes based on historical recounts rather than surficial expressions or direct measurements of their impacts. In recent advances to PTHA, it has become more prevalent to rely on modeling complex earthquake source rupture processes, such as the heterogeneous slip distributions, and use the resulting deformation as the initial condition for propagation modeling. This is then combined with some probabilistic scaling relations as well as earthquake recurrence rates for quantification of likely exceedance of tsunami hazard intensities (e.g. Li et al., 2016; De Risis & Goda, 2017; Grezio et al., 2020).

In this approach to PTHA, arguably, the largest source of uncertainty is the earthquake or tsunami source, since propagation modeling is already highly advanced and bathymetry, both in the deep ocean and in the nearshore, is relatively well-known. Earlier tsunami forecasting methods assumed a uniform slip on a geometrically simple fault buried in a homogeneous elastic half-space. It is now broadly recognized that assuming homogeneous slip drastically underrepresents the tsunamigenic potentials when compared to heterogeneous slip models for the same magnitude (Ruiz et al., 2015; Melgar et al., 2019). The situation is different, however, for inundation modeling of overland flow. Many advances in modeling the fluid dynamics of propagation over an erodible substrate and through the built environment are still necessary and introduce equally, if not larger, sources of uncertainty than knowledge of the earthquake source. However, for the simpler problem of quantifying the expected tsunami at the shoreline, without considering inundation, better constraints on what sources can realistically be expected to occur is one of the improvements that can most significantly reduce uncertainties in the hazard estimate.

In this work we focus on the CSZ as it is extensively studied with a multitude of previously constrained locking models, is well instrumented, and is perceived as having high associated hazards. First, we present the mathematical formalism for introducing a geodetic locking model as a prior constraint on the resulting stochastic rupture. We then model a total of 8400 stochastic slip rupture scenarios for a magnitude range of **M**7.8-**M**9.1 on the CSZ for three distinct cases. Two cases include different end member locking models from Schmalzle et al. (2014) that vary in terms of how much near-trench locking they image (noted as the “Gamma” and “Gaussian” locking models). For a third set of ruptures, we produce stochastic slip in the traditional way, where, beyond assuming a down-dip limit of slip, there are no assumptions on where slip can occur, i.e. with no locking model.

For each of the rupture simulations we model tsunami propagation to the coast and analyze the resulting coastal tsunami amplitudes using hazard curves and hazard maps. We show there are stark differences in tsunami intensities between all three models. Most notable is the increase in arrival height at most coastal points observed with either locking model when compared to the scenarios without a locking model. Hazard curves for coastal points and hazard maps detail that with increasing distance north, the variations in hazards become much more distinct, where the coastal points experience much higher tsunami arrivals for the Gamma model than the Gaussian model. We stress that in this work we are not making an authoritative hazard assessment for the CSZ, we have introduced a number of simplifying assumptions, such as an assumed (and likely poorly constrained) Gutenberg-Richter distribution for the likelihood of an earthquake of a certain magnitude. Rather, we simply aim to demonstrate the impacts of conditioning the ruptures with a locking model. It is our hope, however, that the results are convincing enough that future authoritative hazards assessments more formally consider geodetic locking and that our work be used as motivation to better-constrain offshore locking in particular through expanded seafloor measurements. The variability between models that we will show highlights the need for these improvements.

2. Methods

2.1 Geodetic Locking Models:

Fault locking models (e.g. Bürgmann et al., 2005; Konca et al, 2011; Loveless & Meade, 2010; Moreno et al., 2011) are obtained from inversion of surface velocities measured by geodetic techniques such as global navigation satellite systems (GNSS) and tide gauges. Accurately constraining locking models can be done through integrating paleoseismic data (e.g. McCaffrey et al., 2007), however, good paleoseismic records are typically lacking for a given region. In theory, locking models provide an estimate of a fault's present-day ability to move. Locking is typically quantified by the ratio of the on-fault slip rate vs. the long term far-field plate rate (e.g. the convergence rate at a subduction zone). A ratio of 1 is fully locked and represents no current motion along the plate interface during the inter-seismic period, whereas a ratio of 0 indicates aseismic stable sliding (creep). Conversely, locking models also include by definition an estimate of the "slip deficit rate". The locking fraction is therefore the ratio between the slip deficit rate and the local plate convergence rate. Areas that are fully locked, are accumulating a slip deficit fastest, specifically at the plate convergence rate.

The reliability of the calculated locking models is dependent on the abundance, distribution, and timescale of geodetic stations (primarily GNSS). The resolving power of a specific GNSS site falls rapidly with distance. Currently, GNSS coverage of subduction zones worldwide is quite good for the on-shore portion (e.g. Barrientos & perez-Campos, 2018) but is very limited offshore. Seafloor geodetic instrumentation, which was pioneered at the CSZ (Spiess et al., 1998) is currently only widely implemented in Japan (Yokota et al., 2018), however its use is slowly expanding. This lapse in GNSS coverage means that the uncertainty in the recovered interseismic locking, which is largely in the offshore shallow portion of the subduction zone, can be quite high (e.g. Loveless & Meade, 2010, Schmalzle et al., 2014). Due to the sparsity of station coverage, a multitude of non-unique estimations of plate locking can be determined for a region. As a result of this uncertainty, different modeling assumptions will lead to different results for the near-trench locking. Although locking models are non-unique, they currently provide one of the best approaches for understanding the influence of regional slip deficits on rupture heterogeneities in a given area.

In this paper we consider two different locking models (Figure 1) for the CSZ from Schmalzle et al. (2014). Both represent the "decade scale" distribution of locking where the effect of transient slip such as slow slip events is accounted for. The first model uses an a priori assumption that complete locking occurs at the trench to some distance down dip and that at all points along strike locking fraction decreases to free slip by a shape factor, gamma (Wang et al., 2003; further referred to as the "Gamma" locking model). In contrast, the second approach uses a Gaussian distribution of locking with depth, dependent on a model parameter, mean depth, and spread, or standard deviation, of the locking (further referred to as the "Gaussian" locking model). Due to the Gaussian nature of the locking pattern, at shallow depths near the trench, the plate has low locking and is mostly stably sliding. In this model locking is centralized down dip (Figure 1). It is important to note that both of these approaches fit the known on-shore GNSS velocities, tide gauge records, and geologically-derived uplift rates with near identical confidence.

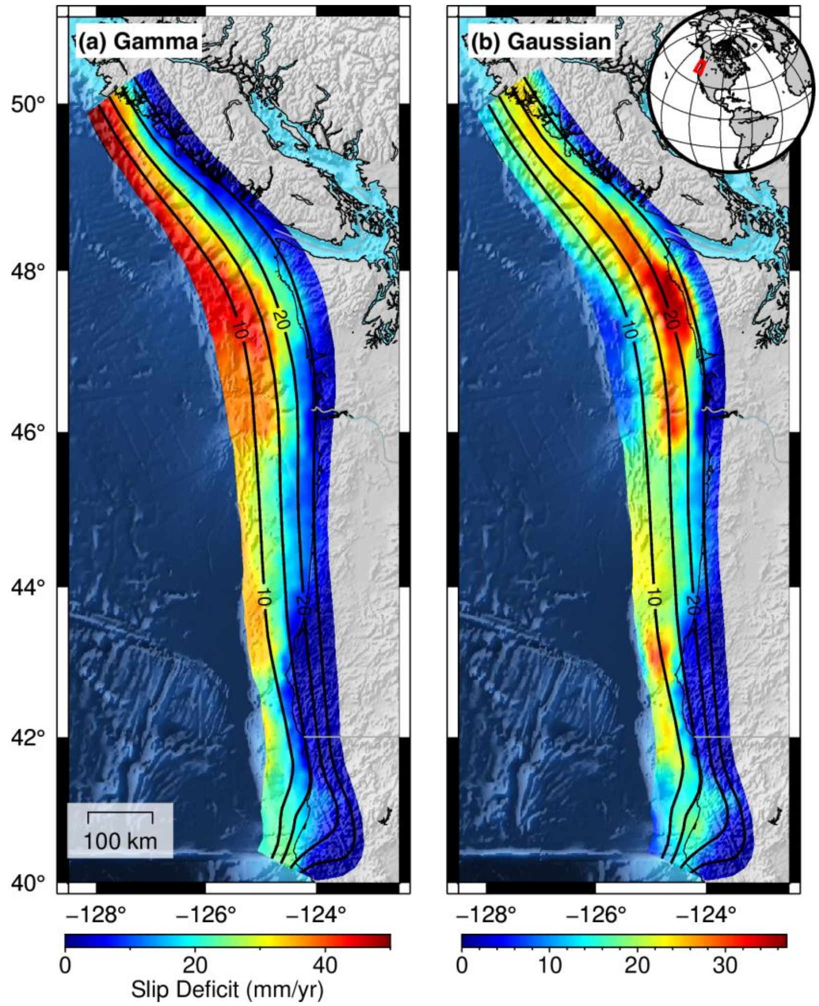

Figure 1: Fault locking models from Schmalzle et al. (2014) for the Cascadia subduction zone. Color scale details slip deficits where a higher value of slip deficit corresponds to areas with the highest locking ratio and a slip rate deficit of 0 mm/yr is freely sliding. (a) Gamma decade-scale locking model assumes the slab is fully locked with large slip rate deficits at the trench and monotonically decays downdip by the shape factor gamma. (b) Gaussian decade-scale locking model imposes a Gaussian distribution of locking with depth as well as penalties to constrain mean locking above 30km in depth. Contours in both panels are the slab depths from Hayes et al. (2018) at 10km intervals. Inset at top right shows the location of the Cascadia subduction zone.

2.2 Stochastic Ruptures with a Geodetic Locking Model Constraint:

The first step in obtaining a rupture model is to determine which portions of the larger megathrust will contribute to a given earthquake. Since our target magnitudes span a range of **M**7.8 to **M**9.1 not all portions of the megathrust will participate in any given rupture. To select a subset of the megathrust we follow the approach detailed in Melgar et al. (2016). Given a target magnitude, we determine the length, *L*, and width, *W*, of the rupture. We make a random draw from probabilistic scaling laws (Blaser et al. 2010) which state that length and width follow the magnitude dependent log-normal distribution with mean and standard deviation given by

$$log_{10}L \sim N(-2.37 + 0.57M\,, \sigma_L) \quad , \quad (1)$$

$$\log_{10}W \sim N(-1.86 + 0.46M, \alpha_w) \quad , \quad (2)$$

with standard deviations defined in the original work. By making these random draws, the objective is to obtain a length and width that is consistent with the behavior seen in earthquakes worldwide while retaining the observed variability as well. The probabilistic scaling law thus ensures that for a given magnitude we do not always employ the same fault dimensions. Once these dimensions are known we randomly select a portion of the larger megathrust models that is within these bounds. An example of this can be seen in Figure 2 and Figure 3 where the fault dimensions for a potential **M**8.7 event have been obtained from the probabilistic scaling laws and used to define a subset of the megathrust to use for the stochastic rupture.

Next we define the rupture model itself. Slip can be conceptualized as a spatially random field whose heterogeneity can be described by statistical parameters. A number of unique slip realizations can then be determined as long as they are constrained by an underlying probability distribution. Mai and Beroza (2002) found that to best model the spatially random slip field the most suitable autocorrelation function (ACF) is the von Karman ACF. In their proposed approach, the von Karman ACF is enforced using a spectral representation, P(k), of slip in the Fourier domain defined as the ratio of the correlation lengths for along-strike (a_x) and downdip (a_z) directions,

$$P(k) = \frac{a_x a_z}{(1+k^2)^{H+1}} \quad . \quad (3)$$

Where the H is the hurst exponent describing the spectral decay at higher wavenumbers. The radial wavenumber, k, is then defined as

$$k = \sqrt{a_x^2\, k_x^2 + a_z^2\, k_z^2} \quad . \tag{4}$$

The correlation lengths described in the von Karman ACF determine the dominant asperity sizes for the model. Here, it is determined that as magnitudes increase, the correlation lengths increase as well following a log-linear scaling (e.g. Melgar & Hayes, 2019). The Hurst exponent in Equation 3 on the other hand, seems to be magnitude independent and typically is assumed to be between 0.4 and 0.7 (Mai & Beroza, 2002, Melgar & Hayes, 2019).

The approach from Mai and Beroza (2002) is well suited for an approximation of a rectangular fault geometry, however, some complexities such as a multi fault or 3D fault geometry (e.g. the large bend in northern CSZ) can be difficult to account for. Similarly, enforcing prior constraints on the rupture model, such as the geodetic locking model, is not inherently straightforward. An alternate approach is to work directly in the spatial domain. LeVeque et al. (2016) use the Karhunen-Loeve (K-L) expansion with the von Karman ACF to the same effect as the spectral approach. The spatial representation of the VK-ACF is used,

$$C_{ij}(r_{ij}) = \frac{G_H(r_{ij})}{G_0(r_{ij})} \quad , \tag{5}$$

$$G_H(r_{ij}) = r_{ij}^H K_H(r_{ij}) \quad , \tag{6}$$

where C_{ij} is the correlation between the i-th and j-th subfaults, K_H is the modified Bessel function of the second kind and H is the Hurst exponent. r_{ij} is the inter-subfault distance given by

$$r_{ij} = \sqrt{(r_s/a_s)^2 + (r_d/a_d)^2} \quad , \tag{7}$$

where r_s is the along-strike distance and r_d the along-dip distance. These are obtained using a spline interpolation of the 3D fault geometry as detailed by Melgar et al. (2016). Once all the parameters of the correlation matrix are defined, the covariance matrix is obtained by

$$\widehat{C_{ij}} = \sigma_i C_{ij} \sigma_j \quad , \quad (8)$$

where $\sigma$is the standard deviation of slip, which we set here to 0.45, irrespective of magnitude, following Melgar & Hayes (2019). The K-L expansion then states that to obtain a random realization the slip vector, *s*, that contains each subfault's slip will be

$$s = \mu + \Sigma_{k=1}^{N} z_k \sqrt{\lambda_k \nu_k} \quad . \quad (9)$$

Here, μ, is the mean of *s* and the statistics of the VK-ACF are enforced by the eigenvalues, λ_k, and eigenvectors,ν_k , of C_{ij} (Equation 8). z_k are normally distributed random numbers with a mean of 0 and a standard deviation of 1 which introduce the desired stochastic variability. *N* is the number of eigenmodes which corresponds to the number of subfaults or elements of *s*. If all the eigenmodes are used, then the stochastic realization produces the same results as if the analysis was carried out in the wavenumber domain. For certain applications, such as PTHA, where long period features dominate the resulting tsunami signals, after the first few tens of modes the contributions to tsunamigenesis from the short length-scale modes becomes negligible (LeVeque et al., 2016). In these cases the summation can be truncated. Here, however, we use all eigenmodes. In the absence of any external knowledge it is commonplace to assume a homogeneous mean slip model, μ. In this case, given the assumed fault dimension and rigidities from the reference Earth model, enough slip is distributed over all subfaults to match the desired target magnitude. In other words, slip is equally likely at all subfaults irrespective of location both along strike and down dip of the fault. Once more, if this is done then the results will be the same as if carrying out the stochastic slip realization in the wavenumber domain. However, here lies the critical advantage afforded by the K-L expansion, we can assume that the mean slip model, μ, is related to, or rather defined by, the geodetic coupling.

The process for defining the mean model, μ, based on the geodetic locking is as follows and is shown in Figure 2. Once a megathrust segment is selected following the probabilistic scaling laws for the desired magnitude (**M**8.7 in the example in Figure 2 and 3) the geodetic coupling (Figure 2a and 3a) is re-scaled to slip (Figure 2b and 3b) to match the target moment. This mean slip model now has the same features as the coupling, with higher slip in high coupling areas and lower slip where coupling is low, and even 0 slip where coupling is 0. Figure

2c and 3c then show 8 realizations of stochastic rupture using the K-L expansion with the non-homogeneous mean model. Note that each realization does not look exactly like the coupling model, but on average slip is more likely where coupling is high, as desired.

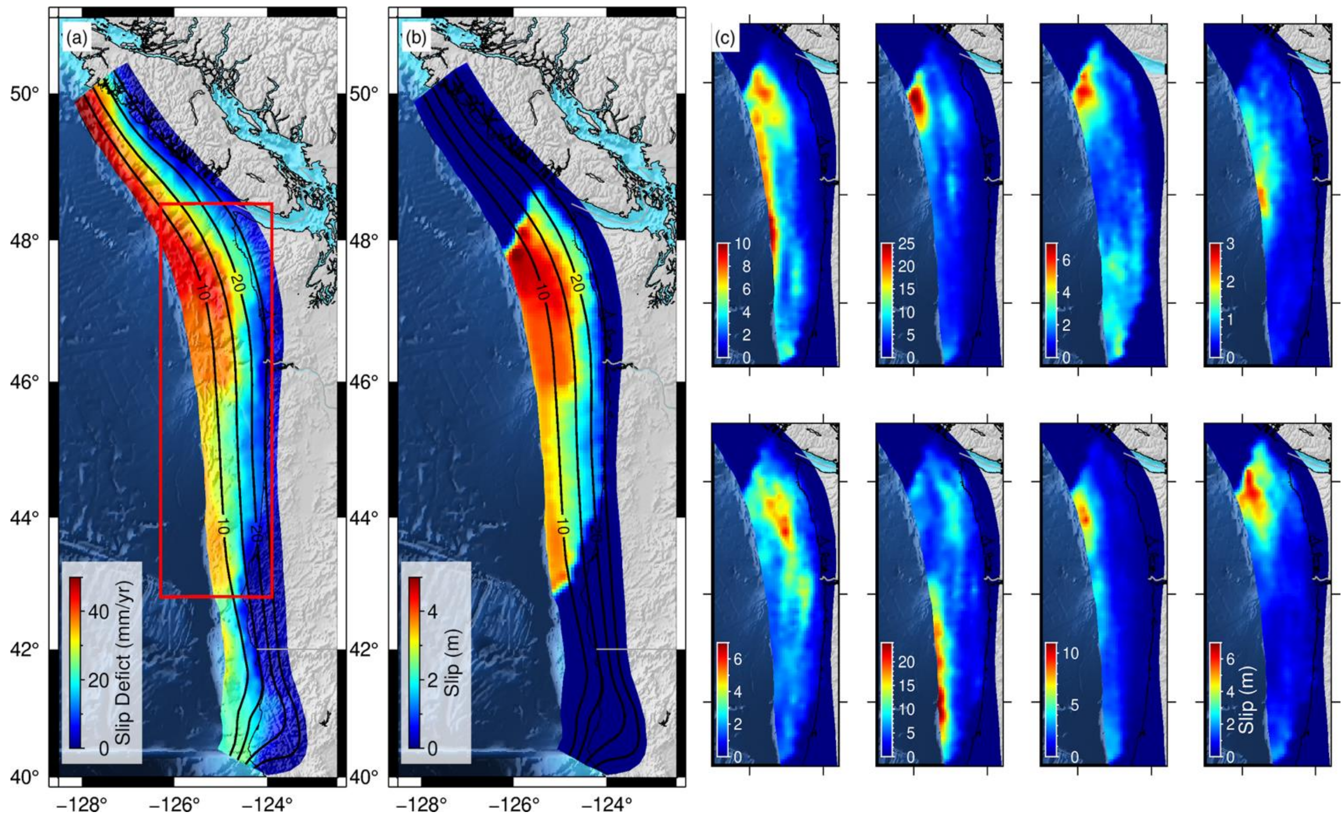

Figure 2: (a) Gamma locking model where the red box outlined contains the area randomly obtained from the probabilistic scaling laws for modeling ruptures. (b) Mean slip determined from the 8 **M**8.7 rupture models imaged on the right. The modeled ruptures are constrained by the same magnitude, correlation lengths, and hypocentral location. The desired mean slip (μ) in the K-L expansion is defined from the Gamma locking model. (c) suite of 8 rupture models all defined by the same rupture area from (a) and the desired mean slip from (b).

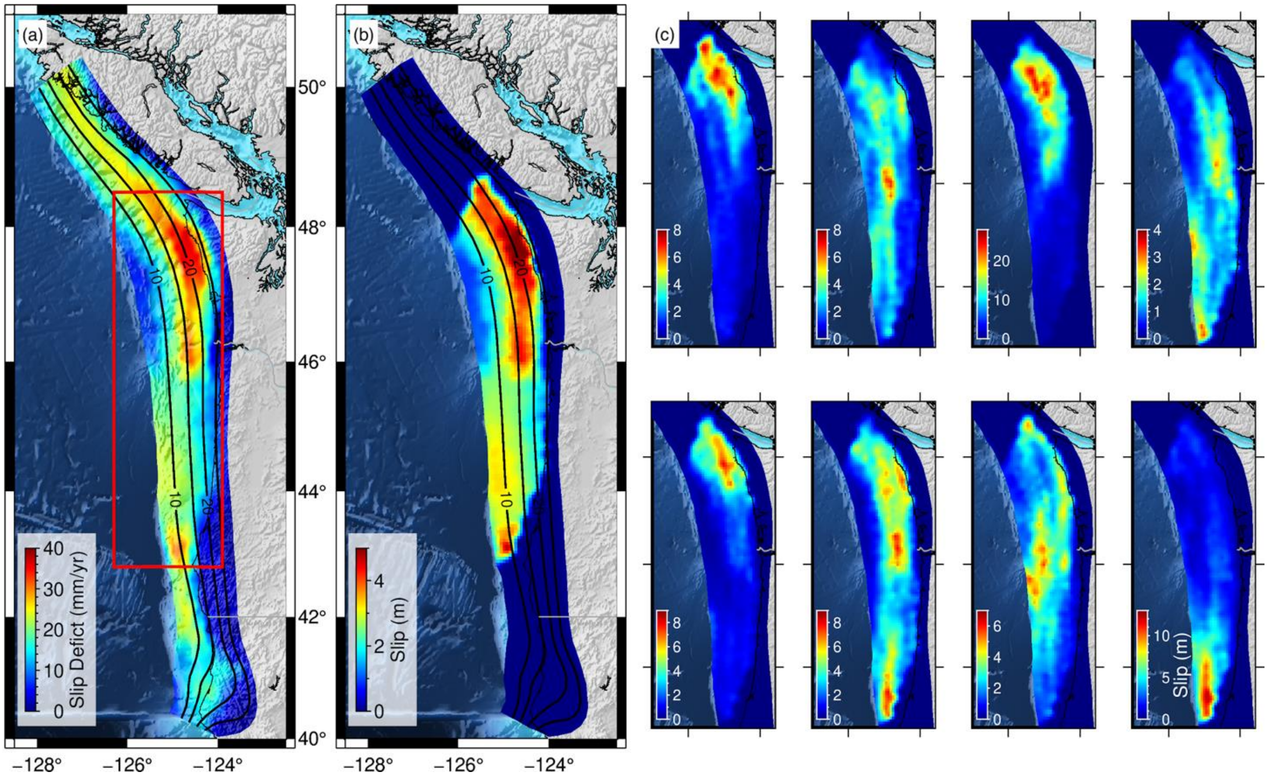

Figure 3: Same as Figure 2 but with the Gaussian locking model included in the rupture modeling.

To carry out these stochastic realizations constrained by a non-homogeneous mean model we modified the open access forward rupture modeling FakeQuakes module which is part of the forward modeling and inversion code MudPy (Melgar & Bock, 2015, Melgar et al., 2016, Melgar, 2020). 200 stochastic slip ruptures for 0.1 magnitude bins ranging between **M**7.8 - **M**9.1 are modeled for the Gamma, Gaussian, and no locking model scenarios (Figure 1). Following the K-L expansion approach, slip on triangular subfaults are determined using all eigenmodes. Ruptures are fixed to the given desired magnitude and have a mean rake of 90 in order to account for pure thrust motion. Following Graves & Pitarka (2015), we introduce some stochastic variability around the rake value as well. The hypocentral location is also randomly assigned from the selected subfaults. The location of the slip area and the hypocentral location are unconstrained, allowing ruptures to be equally likely anywhere along-strike on the megathrust. Additionally, the degree of slip on a single subfault was given an upper bound of 100m of slip.

This allows for ruptures within a given magnitude bin to vary quite drastically between scenarios. Figure 2 and 3 shows one example of the resulting rupture models calculated using the Gamma and Gaussian model implemented in the stochastic rupture modeling. Although the locking model is applied as the desired mean slip, variations in rupture slip patterns and resultant displacements are present and are further discussed later.

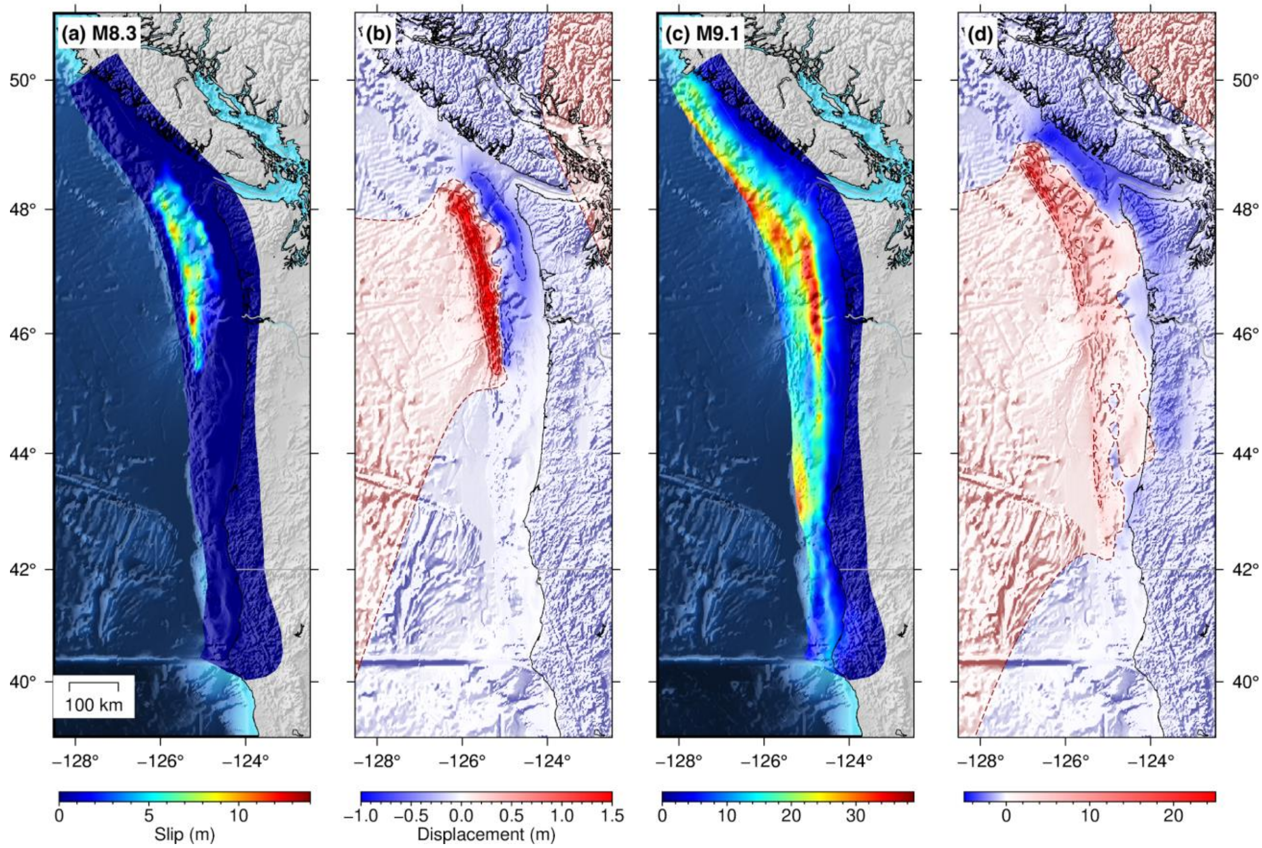

Figure 4: Example rupture scenarios for **M**8.3 and **M**9.1 with implementation of the Gamma decade-scale locking model. Panels (a) and (c) both express total coseismic slip on the fault from each scenario. (b) and (d) express surficial coseismic vertical displacement from the two scenarios. Contours are spaced at 0.5 meters and 5 meters increments for the **M**8.3 and **M**9.1 respectively. Dark red contours map vertical uplift and dark blue maps subsidence.

---

2. 3 Tsunami modeling and Hazard Curves:

For each rupture coseismic vertical displacements at the surface are determined using the analytical solution for angular dislocations for triangular subfaults in an elastic half space (Comninou & Dundurs, 1975). This method is an adaptation from the Okada equations (Okada, 1985), which focus on rectangular subfaults. The resulting vertical deformation patterns for 2 scenarios is depicted in Figure 4. This calculated deformation is then used as the initial condition for tsunami modeling. Here we use the finite volume 2D depth-averaged, non-linear tsunami modeling code GeoClaw (http://www.clawpack.org/geoclaw) (LeVeque et al., 2011). Since rupture propagation velocities are much faster than tsunami wave velocities, we assume instantaneous rupture as the initial condition for the system of partial differential equations. This assumption has a negligible effect on near-source modeling as discussed in Williamson et al. (2019). Topography and bathymetry from the SRTM15 relief model sampled at 15 arcseconds (Tozer et al., 2019) are used in the tsunami modeling. For each scenario we modeled wave propagation for 4 hours after rupture initiation, as we are only interested in the variability of regional arrivals. One of the powerful functions of GeoClaw is the adaptive mesh refinement (AMR) which makes the simulations efficient so that more intricate and complex tsunami characteristics are represented by the finest bathymetric resolution and more simple waves are adaptively coarser. We used 4 levels of refinement with the coarsest level at 3 arcminutes and the finest level at the 15s of the topography/bathymetry data. Time stepping is variable and determined automatically to guarantee numerical stability by enforcing a Courant-Friedrichs-Lewy (CFL) condition of 0.75.

We collect output from the model at 1026 virtual tide gauge points between 39.5° to 50.8° latitude along the coasts of northern California, Oregon, Washington, and Vancouver Island in British Columbia. The gauge points have variable depths offshore, so, in order to homogenize them to a common reference depth we use Green’s law to re-scale the wave amplitudes to 1m depth. Example tsunami models are shown in Figure 5 for the two rupture scenarios detailed prior.

Hazard curves and resulting hazard maps are calculated and reflect the probability of exceedance of tsunami arrival amplitudes for each coastal point over a given return interval. Inherently in the formulation of the hazard curves is the assumption of the time-dependency of earthquake occurrence. We assume a magnitude-time dependent relationship defined by the Gutenberg-Richter (G-R) distribution,

$$N = 10^{(a-b*M_w)} \quad , \qquad (10)$$

where N is the number of yearly events for a given magnitude. The constants a and b are assumed to have values of 6.279 and 1, respectively. These values are used because they produce a return period of 526 years for **M**9 earthquakes. This aligns reasonably well with what is expected for the return period of **M**9 events for the CSZ from the paleoseismic record (e.g. Frankel et al., 2015). After assuming the rates at which earthquakes occur for every coastal location, we compute $P(\eta > \eta_c)$, the probability of the tsunami amplitude at the coast, η, exceeding a given threshold, η_c. Following Geist & Parsons (2006)

$$P(\eta > \eta_c) = 1 - \Pi_{i=1}^{K}(1 - (1 - exp(-N_i t))\, P(\eta > \eta_c\, |M_i) \quad . \qquad (11)$$

Here the product operates over K magnitude bins. 14 in our case for M_i=[7.8,9.1] with 0.1 magnitude units between bins. t is the chosen return interval of interest and N_i is the rate at which earthquakes in a given magnitude bin are assumed to occur from the G-R distribution. Finally, $P(\eta > \eta_c|M_i)$ is the conditional probability that the tsunami exceeds the threshold given that earthquakes of a certain magnitude occur. Following Melgar et al. (2019) This value is obtained empirically from the amplitudes produced at a given point by the 200 tsunami runs in each magnitude bin.

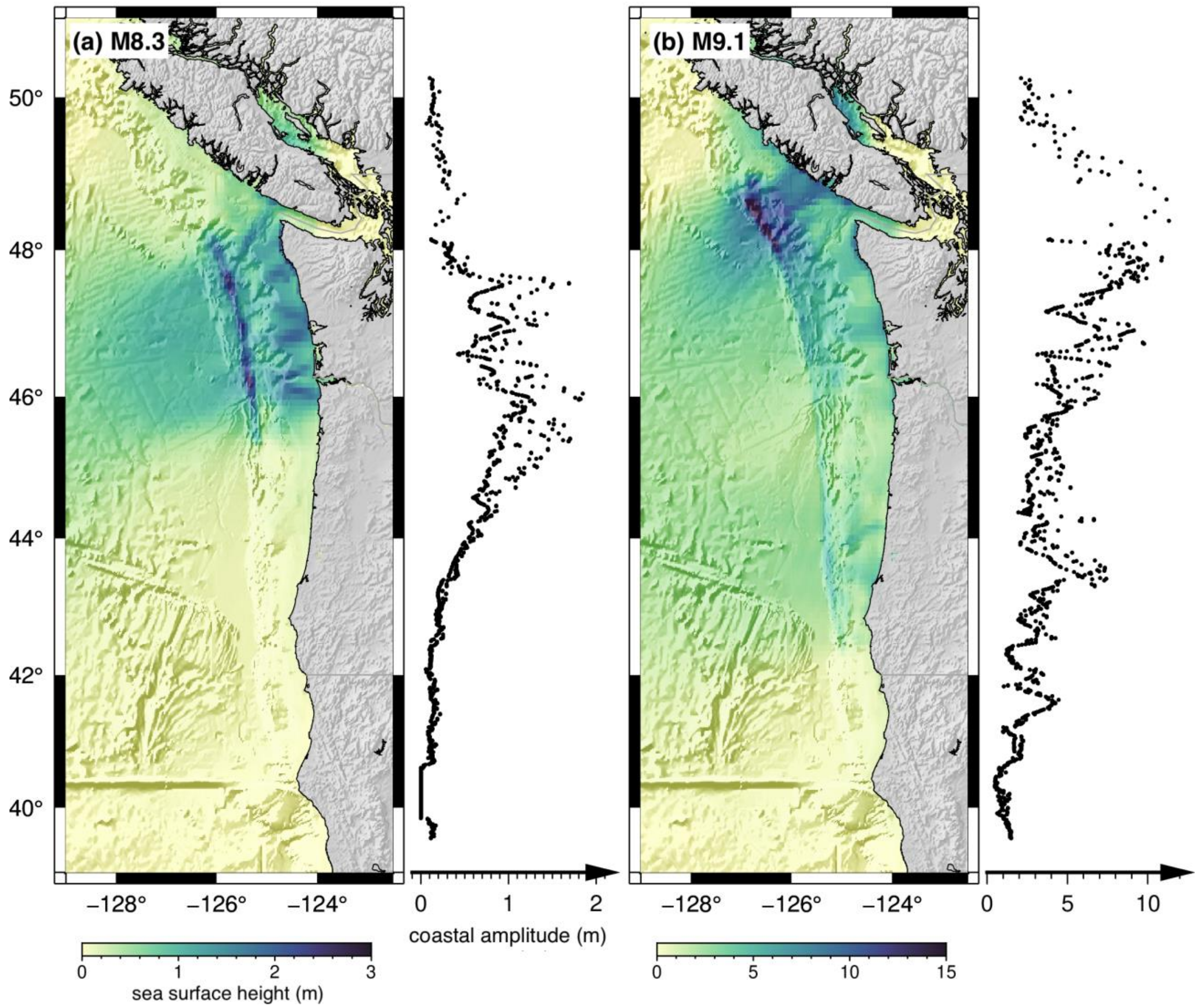

Figure 5: Maximum sea surface heights observed during tsunami model runs for the M8.3 and M9.1 examples from Figure 4. The adjacent scatter plots to each model show the estimated coastal tsunami heights for the 1026 gauge points.

3. <u>Results</u>

Here we present the results of the 8400 rupture scenarios and tsunami models created. Our focus is on highlighting how different assumptions on locking contribute to hazards, so only coastal tsunami amplitudes are considered. We initially present each model separately, highlighting key features so that comparison between model results is clearer.

Although the rupture area and distribution of slip vary in size for a given magnitude bin, both the rupture area and maximum amount of slip on a subfault does on average increase with magnitude for each model following known scaling laws (Figure 6). At larger magnitudes, events begin to saturate in both length and width due to the actual CSZ fault dimensions. As a result of the von Karman ACF, slip is focused around asperities of favorable length scales, and as stated prior, asperity size predominantly scales with increasing magnitude. The stochastic nature of the models partitions and redistributes the asperities throughout the rupture extent. Irrespective of the presence of locking models, ruptures varied between one another. Inherent to the stochastic nature of the rupture modeling, presence and influence of the locking models is not always immediately obvious for an individual rupture; however, when all ruptures were combined into an averaged slip model, the result subsequently resembles the given desired mean slip model μ (Figure 2c and 3c).

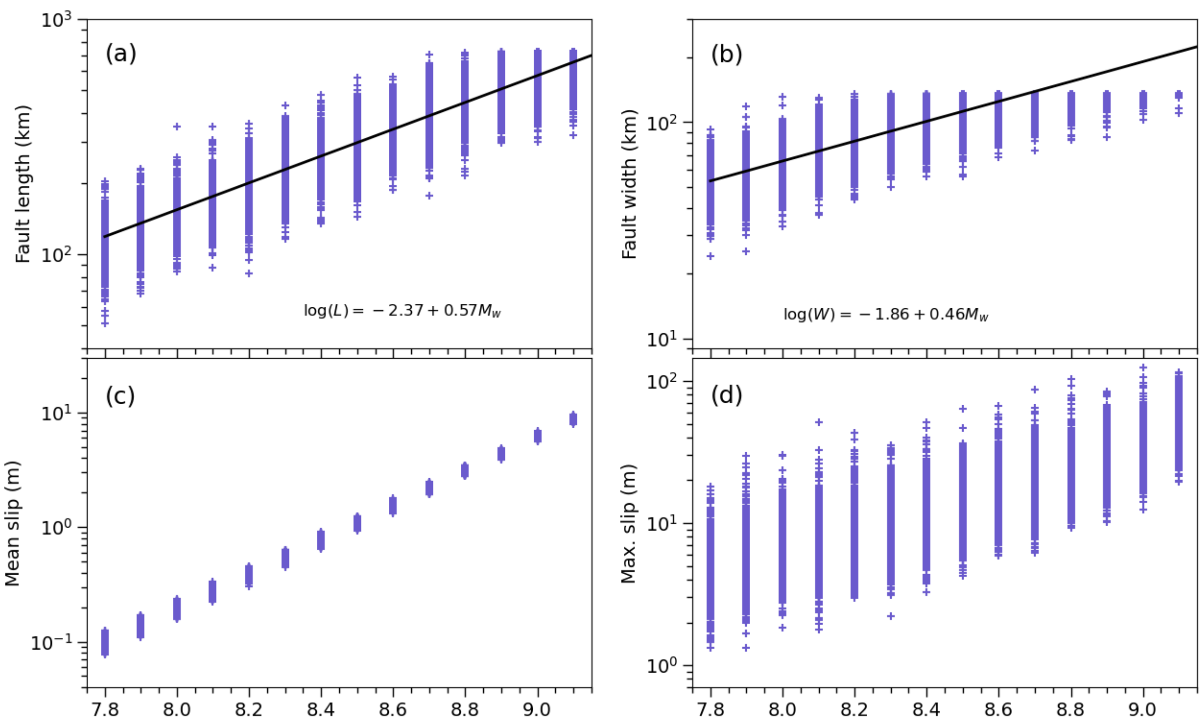

Figure 6: statistical summary of all ruptures generated, regardless of model. (a) fault length, (b) fault width, (c) mean slip of all subfaults, (d) and maximum slip. The black line in panels (a) and (b) are the scaling laws for length and width of rupture from Blaser et al. (2010).

Figure 7 shows summary violin plots of the coastal amplitudes for each of the locking models assumed and for the no locking model case. Each violin represents the kernel density estimate of the distribution of tsunami heights that is possible for a magnitude range at that specific point. Unsurprisingly, within all models calculated, the coastal tsunami arrivals on average increase in response to increasing rupture magnitude irrespective of the coastal latitudinal location. At lower magnitude scenarios (e.g **M**7.9) arrival height differences are not as obvious between models. Once magnitudes become great enough and larger swaths of the megathrust participate, differences in the coastal amplitudes that correlate to the particularities of the assumed locking model become more obvious. The southern extent (below 43° latitude) of the study area on average experiences smaller variations between models, even at larger magnitudes. However, the resulting tsunami amplitude variations become prominent in the northern extent (46°- 48° latitude) of the study area off the coast of Washington. In this region, the slab orientation begins to bend, the distance between the trench and the coast increases, and the most obvious variations in depth of maximum slip deficit occur.

The Gamma scenarios, which assume larger and shallower offshore locking, experience the most drastic differences in tsunami arrival heights between the northern and southern extent of the coasts in comparison with the other two models. The fully locked zone in the Gamma model may extend throughout the entirety of the trench, but the total area of full locking is widest starting at about 46° latitude and continuing to the edge of the study area. This separation matches well with the divide between the two regions of southern and northern arrival heights. At **M**9.1, the arrival mean differences between the two regions is ~3m in the southern region and almost ~6m on average in the northern region.

Unlike the Gamma model, there does not appear to be any clear separation of zones of high and low estimated tsunami amplitudes for the Gaussian locking model. Interestingly, the Gaussian decade-scale locking model contains a prominent region of locking apparent in both the southern and northern region of the subduction zone; yet unlike the Gamma model, locking here occurs between 15-25km downdip at its highest locking ratio. There is a clear deficiency of slip along the trench in the northern region in comparison to the Gamma model. Although large slip occurs closer to the coast in these scenarios, it also occurs much deeper than the previous models, limiting the surface displacement response and therefore producing a smaller volume of displaced water leading to overall smaller amplitude tsunamis. Amplitude means for the Gaussian model vary by only 1m at most between the two regions.

Similar to the Gaussian model, the model without any imposed heterogenous locking does not see a prominent distinction between regions for the tsunami arrivals. There is a slight increase in the amplitude of arrivals in the northern gauge points than the southern (Figure 7), similar to but less obvious than in the previous two models. Mean recorded gauge point amplitudes do not exceed 5m even for **M**9.1 events. Since these models lack any form of constraints to favor slip along the slab interface, there is no distinction in the probability of activation of slip at any given subfault. With that in mind, mean consequential tsunamis arrivals should only vary due to the bathymetry and shape of the coastlines and should therefore have smaller variability laterally along the coast as a result of the ruptures themselves.

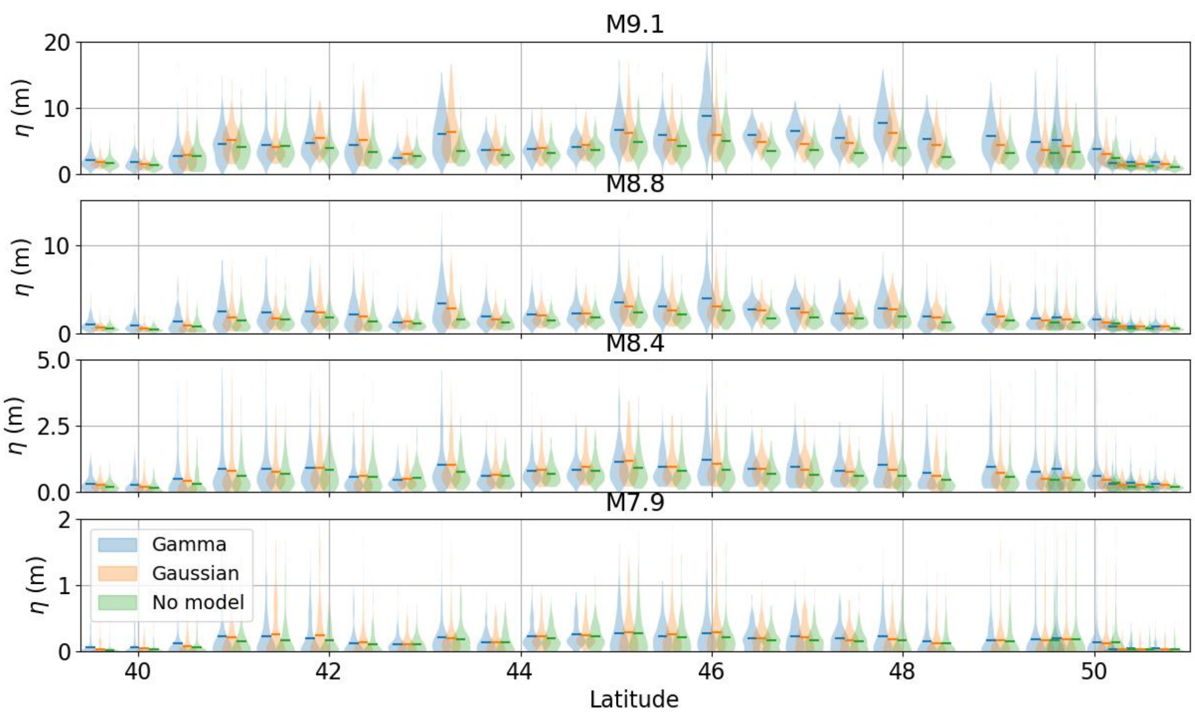

Figure 7: Violin plots showing the spread of the coastal amplitude, η, for selected virtual tide gauge points. Central bar for each model is the mean value of arrivals for the given magnitude bin. Vertical axis varies but increasing arrival amplitudes are recorded for all three models.

---

4. Discussion

The ruptures created varied considerably between model runs for any given magnitude bin. The two different assumed locking models clearly show differences in the depth dependence of slip. Figure 8 depicts three depth-averaged slip cross-sections for each assumed locking model for all **M**8.8-**M**9.1 ruptures. As expected, the ruptures with a homogeneous mean model (no assumed locking) contain almost no depth dependency for slip. This then allows slip to propagate as deep as the model area extends (~30km) and therefore slip is as probable to occur in these downdip regions as it is close to the trench. Meanwhile, for the cases where a locking pattern is imposed, there is a clear connection between the amount of slip and depth of the slab. The depth dependency of both the ruptures with imposed Gamma and the Gaussian locking models becomes synonymous to the distribution of locking for the two regions. In the northern and southern regions of the CSZ where slip deficit is the highest for both models, a dominantly monotonic decrease in amount of slip is seen for the Gamma model and pseudo-Gaussian slip shape is seen for the Gaussian model. As a result of this, the Gamma model experiences far greater slip shallower in depth when compared to the other two models, directly affecting the tsunami generation as seen in the hazard curves and the hazard map (Figure 9 and 10). Areas associated with the smallest locking ratio see very little slip, predominantly in the southern region of the CSZ. Along strike variations in slip concentration are also present between the models where locking is included (Figures 2, 3, and 8).

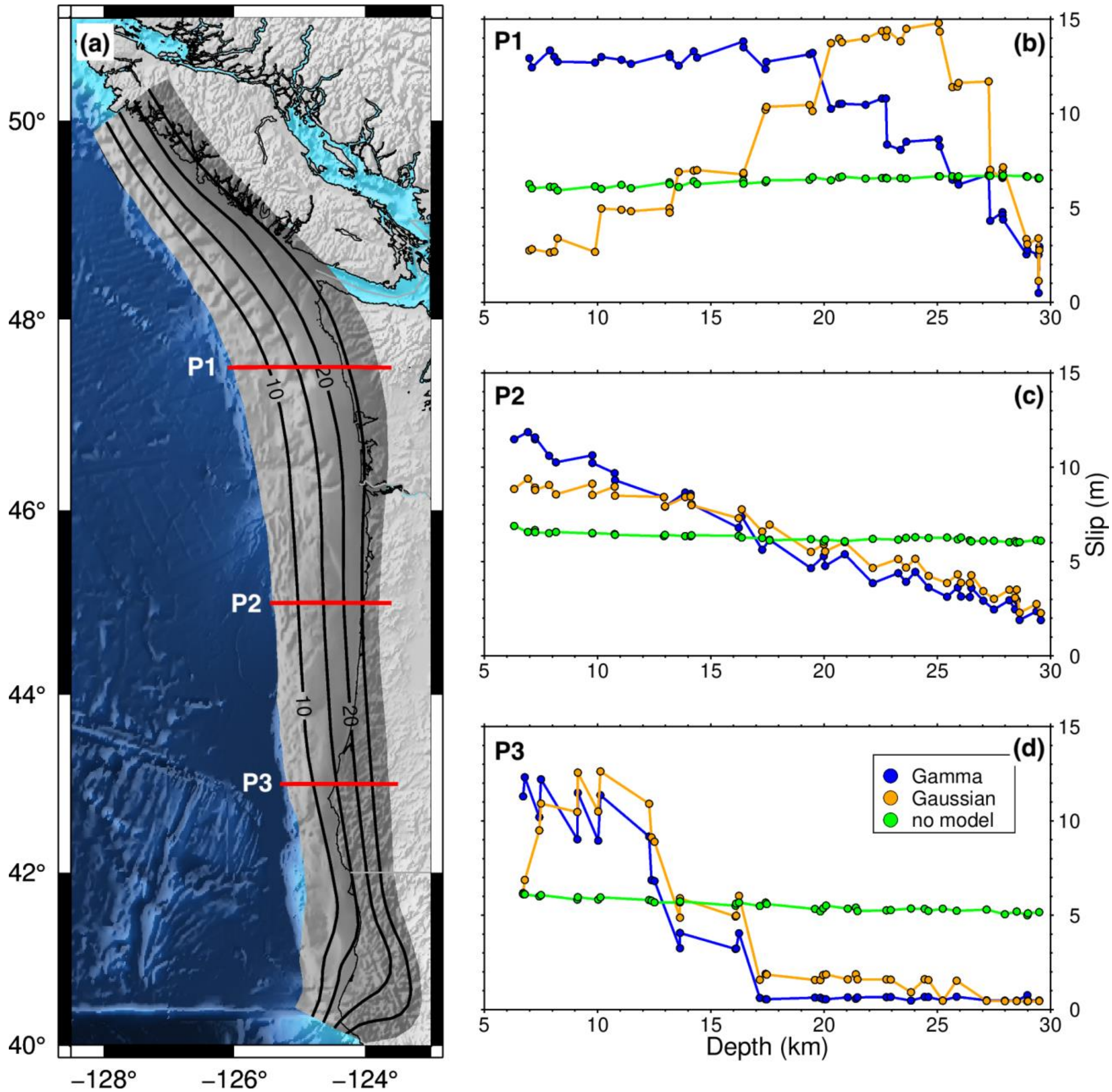

Figure 8: Mean slip as a function of depth. (a) Cascadia subduction zone, with depth of slab contour intervals at 5 km. Red horizontal lines labeled P1, P2, and P3 depict the locations of the three profiles in the adjacent plots at 47.5°, 45°, and 43° latitude. (b) Depth of slab versus mean slip from the three models for 800 ruptures for each model between **M**8.8 - **M**9.1 between 47.3° and 47.7° latitude. Gamma, Gaussian, and the model without locking included are depicted as orange, blue, and green, respectively. Points on each line are the model values at each triangular subfault in the region. (c) The same as (b) but for the region of 44.8° to 45.2°. (d) same as previous but for the region of 42.8° to 43.2°.

Similarly, it is important to reiterate that the locking fraction does not perfectly correlate to where the slip occurs for any given rupture. Rather, the locking as implemented here (Equation 9) will define regions where slip is more likely or less likely to occur. Since there is a sparse record of the earthquake history of the CSZ, locking should only be used as a first order constraint. Further research on more earthquake cycles, past and future, will then allow us to better constrain the accuracy and applicability of locking as it relates to the rupture characteristics.

Additionally, in our implementation we have assumed that a locking ratio of 0 (fully creeping) corresponds to parts of the megathrust that cannot participate in the coseismic process. However, recent modeling studies have argued that dynamic effects can push the rupture into transition regions of the subduction zone. Areas of 0 coupling may, under certain circumstances, participate seismically (Ramos et al. 2019). An example in recent is the July 2020 **M**7.8 earthquake off the Alaskan-Aleutian arc is believed to have ruptured in the eastern portion of the previously assumed, seismically uncoupled Shumagin Gap (Crowell & Melgar, 2020).Observational studies have also shown potential overlap between regions with slow slip and regions with coseismic slip (e.g. Lin et al., 2020). However, since the dynamic effects and their influences in rupture propagation into transition zones are not yet well understood in terms of what controls them and how to quantify their likelihood of occurrence, we do not include them in the rupture modeling process. This has little effect on PTHA since shallow slip contributes far more to the overall hazard. However, for other applications it is potentially important as it would allow for slip further inland and closer to large population centers on the CSZ.

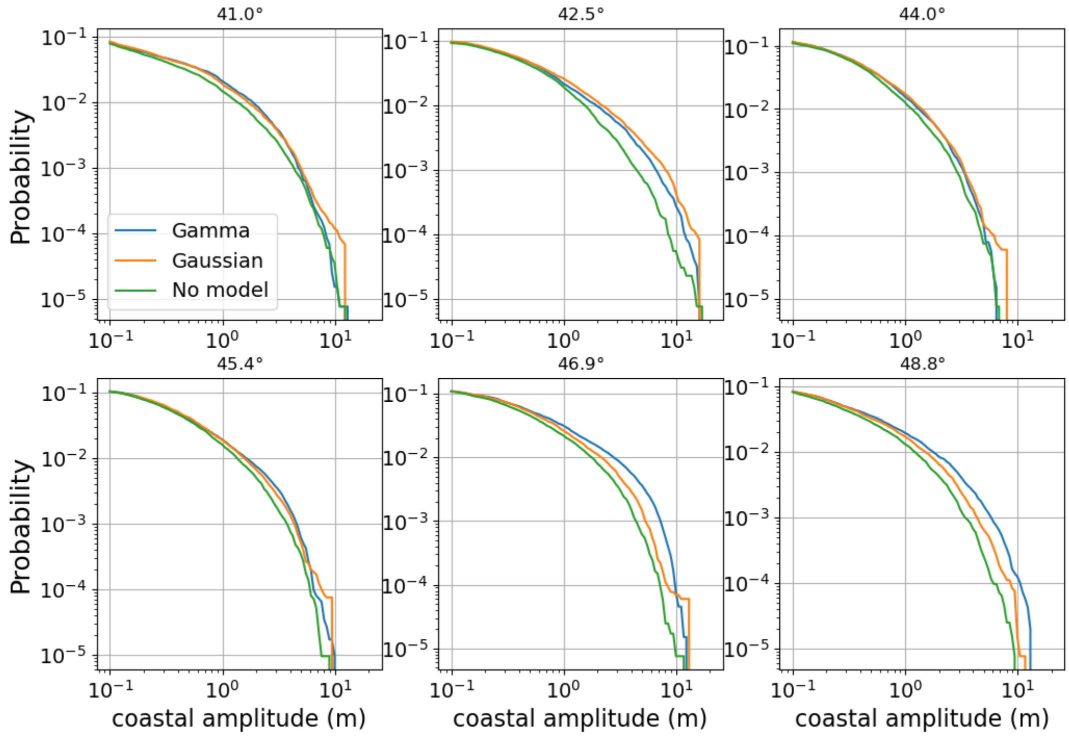

Figure 9: Hazard curves of a 1 year return period for six coastal gauge points with locations depicted in Figure 10. The three distinct models are colored accordingly. Curves are determined using a magnitude time distribution defined by the Gutenberg-Richter scaling relation and the method is described previously. Model variations in hazard probabilities become most visible in the northern extent of the subduction zone.

Following the rupture model patterns, the associated tsunami hazards tend to increase towards the north of the study area. Figure 9 shows hazard curves at 6 coastal locations (shown in Figure 10) for a 1 year return period. These curves give a good quantitative measure to the associated tsunami hazards for the rupture models. Although these are site specific, it becomes quite clear that there are pronounced effects in the associated hazards when locking is included in modeling. For all 6 sites, including either of the two locking patterns increases the probability of a larger tsunami amplitude for the given return period. In the southern and central CSZ, however, the associated hazards are similar between locking models. Recall that in the central portion of the subduction zone interface between 44°-46° latitude (Figure 1), the slip deficit is much smaller, and therefore the locking ratio is much smaller. However, for both the locking models the associated hazards are significantly higher than the case where no locking model is assumed (Figure 10).

The majority of coastal points do see a significant variation between the two models with locking, however, the northern region along the state of Washington experiences the largest differences in tsunami amplitude probabilities. 2% probability of exceedance in 50 years hazard maps for the three models are depicted in Figure 10. The stark difference in amplitudes in the north highlights the effects the locking models have on the ruptures. Below 46° latitude the Gaussian and Gamma locking models are not as clearly distinct from one another. Above, where the slab bends and the slab dip shallows, locking varies more noticeably, with the strongest locking for the Gaussian model occurring around 20km depth and the Gamma model is strongly locked from 15km all the way to the trench. With larger and shallower locking regions in the Gamma model, more slip is observed closer to the trench (Figure 8) and therefore the resulting tsunamis appear much larger.

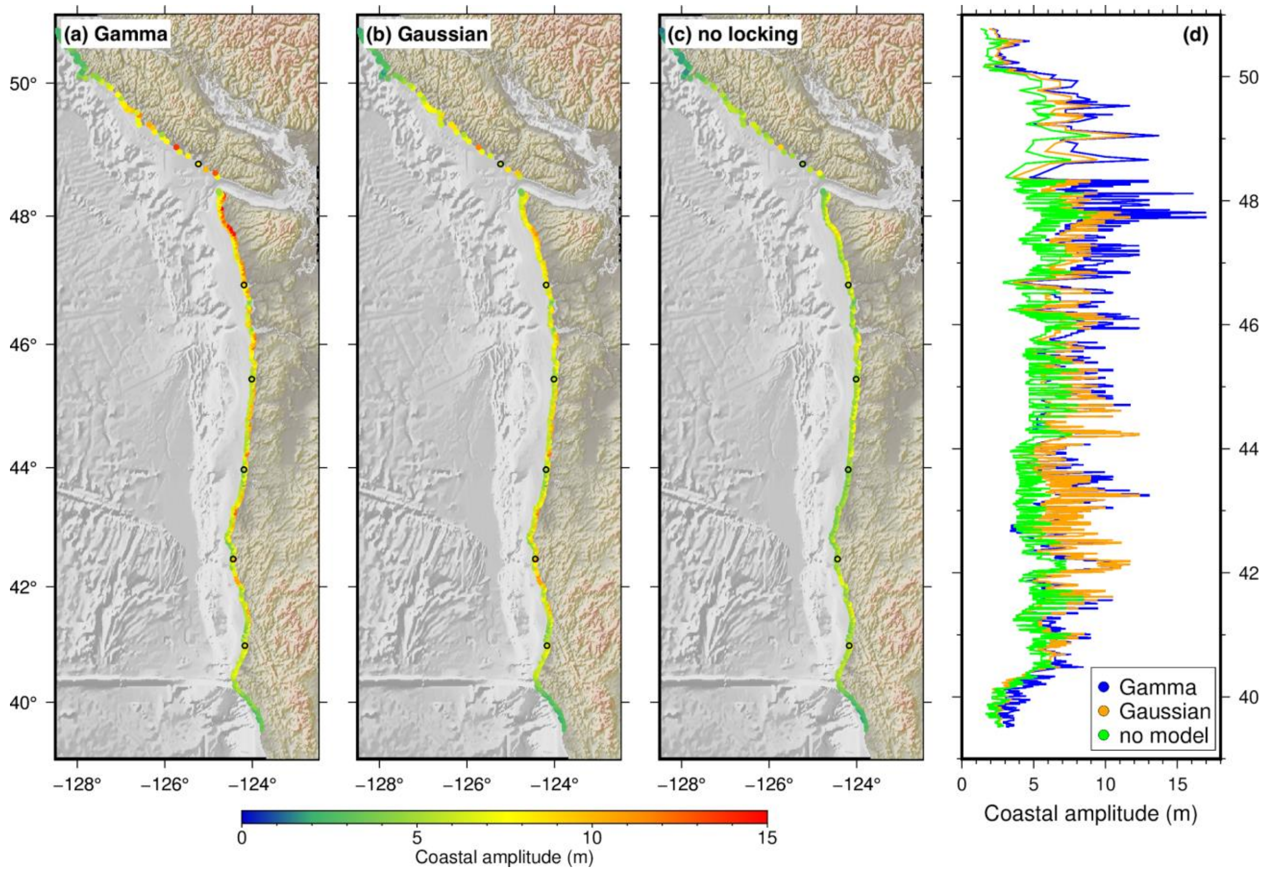

Figure 10: Hazard maps for the three models showing the 2% probability of tsunami threshold exceedance for a 50 year return period at each of the 1026 modeled coastal gauge points. (a) Gamma locking model, (b) Gaussian locking model, and (c) no locking model. Color scale describes η for each gauge point. (d) η at each gauge point location in latitude for the three models.

The hazard variability along strike observed in the stochastic slip models without imposed locking is associated with variations present in the tsunami propagation path and the site conditions (the shape of the coastline). These variations are dominantly controlled by the bathymetry and distance from the tsunami initiation loci to the coast. The influence of the surficial expressions in hazard generations are the only sources of variability for the control model, whereas the models with locking are more complex. Around 44° latitude, the distance of the trench to the coast begins to widen quite drastically and the bathymetry becomes more heterogeneous over a larger distance. The estimated tsunami amplitude for gauge points south of 44° are on average noticeably smaller than those north.

One important point for assessing tsunami hazards in this way is whether the 200 ruptures simulated for each magnitude bin are sufficient to capture all the possible variability in the resulting tsunamis. In order to assess the statistical stability of the models, we refer to Figure 11 where the conditional probabilities, $P(\eta > \eta_c | M_i)$, are plotted for four magnitude bins against the number of scenarios observed. The conditional probabilities are relatively stable even after only ~100 scenarios are included, however, our results detailed prior are determined using all 200 scenarios. Although here we plot the Gamma locking model, the results are similar for the two other models. A formal CSZ hazard assessment should consider whether the stability observed in these conditional probabilities is sufficient or whether more scenarios are needed.

We note as well that we have assumed a fairly simple geometry for the shallow most megathrust with no splay faults. These have been inferred to exist in the CSZ (Booth-Rea et al., 2008) and coseismic motion on them can have a significant effect on the resulting tsunami (e.g. Gao et al., 2018). Similarly, we have considered only simple elastic deformation. Distributed deformation of the heavily sedimented deformation front (Han et al., 2017) could affect the ensuing tsunami as has been noted in places like Indonesia (Hill et al., 2012). Likewise, plastic deformation of the wedge can increase the amount of vertical deformation and lead to larger than expected tsunami (Ma & Nie, 2019).

The results discussed above are a compelling argument to include the influence of locking for both the possible slip and rupture geometry generated as well as the subsequent tsunami hazards. However, without stronger confidence in the specifics of the locking for the region, large uncertainties are still present. The two locking models included here differ significantly, especially in the near-trench region. There is currently no way to distinguish between them because they produce the same onshore inter-seismic velocity field (Schmalzle et al., 2014). Additionally, there are other potential locking models for the region (e.g Li & Liu, 2016; Michel et al., 2019) which include different assumptions, such as long-term viscoelastic relaxation of the upper mantle. Nonetheless, the two models we have used here, can be thought of as depicting two end member cases of the possible locking distribution throughout the CSZ. The other existing locking models share similar features to either of these two. This large uncertainty between models highlights the necessity of the community to further seafloor instrumentation and seafloor geodesy in order to constrain the shallow locking. Constraining locking using hybrid modeling of both on land and seafloor geodetic instrumentation has already been implemented for the Nankai Trough along the coast of Japan (Yokota et al., 2016). Use of the locking model present by Yokota et al. (2016) has also been implemented in tsunami wave propagation modeling from the two Kii Peninsula earthquakes of 2004 (Watanabe et al., 2019).

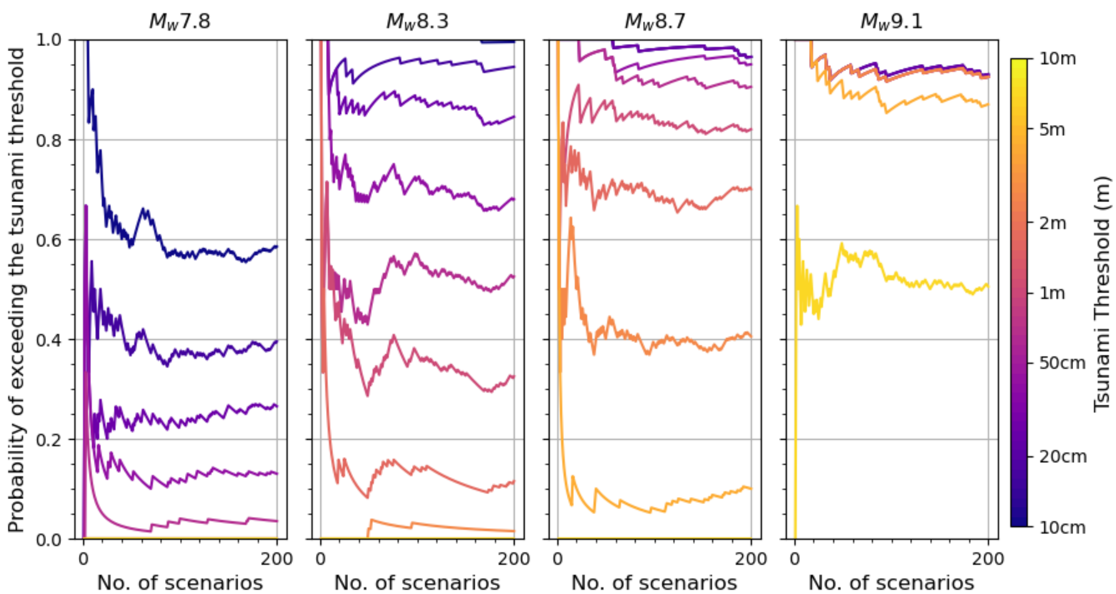

Figure 11: Conditional probability of exceeding the tsunami threshold given that a number of scenarios has occurred for a given magnitude using the Gamma models, $P(\eta > \eta_c|M_i)$. Four different magnitude bins are depicted, all plotted for the gauge point at 46.9° latitude (Figures 9 & 10). The Gaussian and the no locking model produce similar probable stabilities at around 100 scenarios.

Finally, we note once more that these results should not be used as an authoritative hazard assessment for the CSZ. Further work remains to be done in order to improve accuracy for future applications: we have used a number of simplifying assumptions, considered only one kind of tsunami source, and cannot at this point distinguish which of the two locking models is more likely. Our results instead highlight the large variations in rupture patterns and the resultant tsunami hazards created by including inter-seismic locking, a key property of the megathrust. This shows that disregarding important information, like inter-seismic locking, in rupture modeling can lead to hazards estimates that are potentially underestimated.

5. Conclusion

Current stochastic rupture modeling techniques do not consider the influence of first order fault zone characteristics like inter-seismic locking. A correlation between high slip patches and areas of greatest locking ratios has been noticed for recent large earthquakes on megathrusts globally and suggests that this information should be taken into account. Here we presented an updated mathematical formalism to introduce locking models as prior information into stochastic rupture modeling. We compared two end member models of locking, one with a fully locked zone extending to the trench and another with locking deeper downdip and determined the variable influence that this has on the resulting rupture models. Large variations in slip distribution are present in the rupture models and correlate well with areas with the largest differences in slip deficit. We found that when compared to typical stochastic slip ruptures without imposed locking, on average, more slip is produced at shallower depths. To exemplify the importance of this the ruptures were then used in a probabilistic tsunami hazard assessment of the CSZ. We found that the tsunami amplitudes generated are larger throughout the region when locking is used to condition the rupture models. More specifically, in the northern extent of the CSZ, associated hazards are much larger where differences in locking distribution are more drastic. Although large uncertainties are present in the accuracy of modeled locking, imposing either constraint created very different hazard estimations when compared to the hazard estimations when no locking prior information was used. To bridge the uncertainties in present inter-seismic locking and therefore refine our knowledge of first order fault characteristics for future hazard assessments, expanded seafloor instrumentation is vital.

Data availability Statement

The FakeQuakes module used to generate the ruptures is part of the MudPy package archived at Zenodo and can be found online (https://doi.org/10.5281/zenodo.3703200). The SRTM15+ bathymetry can be obtained from https://topex.ucsd.edu/WWW_html/srtm15_plus.html. GeoClaw software for modeling geophysical flows over topography can be found online (http://www.clawpack.org/geoclaw).

Acknowledgments

This work was funded by NSF Graduate Research Fellowship Program grant No. NSF16104 and NSF grant OAC-1835661. Partial support is also from NASA grants 80NSSC19K0360 and 80NSSC19K1104 We'd like to thank Amy Williamson and Dara Goldberg for helpful discussions on rupture and tsunami modeling.

References

Barnhart, W. D., Murray, J. R., Briggs, R. W., Gomez, F., Miles, C. P., Svarc, J., ... & Stressler, B. J. (2016). Coseismic slip and early afterslip of the 2015 Illapel, Chile, earthquake: Implications for frictional heterogeneity and coastal uplift. *Journal of Geophysical Research: Solid Earth*, *121*(8), 6172-6191.

Barrientos, S., & Pérez-Campos, X. (2018). Preface to the Focus Section on Geophysical Networks and Related Developments in Latin America. *Seismological Research Letters*, *89*(2A), 315-317.

Blaser, L., Krüger, F., Ohrnberger, M., & Scherbaum, F. (2010). Scaling relations of earthquake source parameter estimates with special focus on subduction environment. *Bulletin of the Seismological Society of America*, *100*(6), 2914-2926.

Bijelić, N., Lin, T., & Deierlein, G. G. (2018). Validation of the SCEC Broadband Platform simulations for tall building risk assessments considering spectral shape and duration of the ground motion. *Earthquake Engineering & Structural Dynamics*, *47*(11), 2233-2251.

Booth-Rea, G., Klaeschen, D., Grevemeyer, I., & Reston, T. (2008). Heterogeneous deformation in the Cascadia convergent margin and its relation to thermal gradient (Washington, NW USA). *Tectonics*, 27(4).

Bürgmann, R., Kogan, M. G., Steblov, G. M., Hilley, G., Levin, V. E., & Apel, E. (2005). Interseismic coupling and asperity distribution along the Kamchatka subduction zone. *Journal of Geophysical Research: Solid Earth*, *110*(B7).

Comninou, M., & Dundurs, J. (1975). The angular dislocation in a half space. *Journal of Elasticity*, *5*(3-4), 203-216.

De Risi, R., & Goda, K. (2017). Simulation-based probabilistic tsunami hazard analysis: empirical and robust hazard predictions. *Pure and Applied Geophysics*, *174*(8), 3083-3106.

Field, E. H., Jordan, T. H., Page, M. T., Milner, K. R., Shaw, B. E., Dawson, T. E., ... & Weldon, R. J. (2017). A synoptic view of the third Uniform California Earthquake Rupture Forecast (UCERF3). *Seismological Research Letters*, 88(5), 1259-1267.

Frankel, A., Chen, R., Petersen, M., Moschetti, M., & Sherrod, B. (2015). 2014 update of the Pacific Northwest portion of the US National Seismic Hazard Maps. *Earthquake Spectra*, 31(S1), S131-S148.

Frankel, A., Wirth, E., Marafi, N., Vidale, J., & Stephenson, W. (2018). Broadband Synthetic Seismograms for Magnitude 9 Earthquakes on the Cascadia Megathrust Based on 3D Simulations and Stochastic Synthetics, Part 1: Methodology and Overall ResultsMethodology and Overall Results. *Bulletin of the Seismological Society of America*, *108*(5A), 2347-2369.

Gao, D., Wang, K., Insua, T. L., Sypus, M., Riedel, M., & Sun, T. (2018). Defining megathrust tsunami source scenarios for northernmost Cascadia. *Natural Hazards*, 94(1), 445-469.

Geist, E. L., & Parsons, T. (2006). Probabilistic analysis of tsunami hazards. *Natural Hazards*, *37*(3), 277-314.

Goldberg, D. E., & Melgar, D. (2020). Generation and validation of broadband synthetic P waves in semistochastic models of large earthquakes. *Bulletin of the Seismological Society of America*, *110*(4), 1982-1995.

Graves, R., Jordan, T. H., Callaghan, S., Deelman, E., Field, E., Juve, G., ... & Okaya, D. (2011). CyberShake: A physics-based seismic hazard model for southern California. *Pure and Applied Geophysics*, *168*(3-4), 367-381.

Graves, R., & Pitarka, A. (2015). Refinements to the Graves and Pitarka (2010) broadband ground-motion simulation method. *Seismological Research Letters*, *86*(1), 75-80.

Grezio, A., Babeyko, A., Baptista, M. A., Behrens, J., Costa, A., Davies, G., ... & Harbitz, C. B. (2017). Probabilistic tsunami hazard analysis: Multiple sources and global applications. *Reviews of Geophysics*, 55(4), 1158-1198.

Grezio, A., Cinti, F. R., Costa, A., Faenza, L., Perfetti, P., Pierdominici, S., ... & Selva, J. (2020). Multisource Bayesian Probabilistic Tsunami Hazard Analysis for the Gulf of Naples (Italy). *Journal of Geophysical Research: Oceans*, *125*(2), e2019JC015373.

Han, S., Bangs, N. L., Carbotte, S. M., Saffer, D. M., & Gibson, J. C. (2017). Links between sediment consolidation and Cascadia megathrust slip behaviour. *Nature Geoscience*, 10(12), 954-959.

Hill, E. M., Borrero, J. C., Huang, Z., Qiu, Q., Banerjee, P., Natawidjaja, D. H., ... & Li, L. (2012). The 2010 Mw 7.8 Mentawai earthquake: Very shallow source of a rare tsunami earthquake determined from tsunami field survey and near-field GPS data. *Journal of Geophysical Research: Solid Earth*, 117(B6).

Konca, A. O., Hjorleifsdottir, V., Song, T. R. A., Avouac, J. P., Helmberger, D. V., Ji, C., ... & Meltzner, A. (2007). Rupture kinematics of the 2005 Mw 8.6 Nias–Simeulue earthquake from the joint inversion of seismic and geodetic data. *Bulletin of the Seismological Society of America*, *97*(1A), S307-S322.

Konca, A. O., Avouac, J. P., Sladen, A., Meltzner, A. J., Sieh, K., Fang, P., ... & Natawidjaja, D. H. (2008). Partial rupture of a locked patch of the Sumatra megathrust during the 2007 earthquake sequence. *Nature, 456*(7222), 631-635.

LeVeque, R. J., George, D. L., & Berger, M. J. (2011). Tsunami modelling with adaptively refined finite volume methods. *Acta Numerica*, *20*, 211.

LeVeque, R. J., Waagan, K., González, F. I., Rim, D., & Lin, G. (2016). Generating random earthquake events for probabilistic tsunami hazard assessment. In *Global Tsunami Science: Past and Future, Volume I* (pp. 3671-3692). Birkhäuser, Cham.

Li, L., Switzer, A. D., Chan, C. H., Wang, Y., Weiss, R., & Qiu, Q. (2016). How heterogeneous coseismic slip affects regional probabilistic tsunami hazard assessment: A case study in the South China Sea. *Journal of Geophysical Research: Solid Earth*, *121*(8), 6250-6272.

Li, S., & Freymueller, J. T. (2018). Spatial variation of slip behavior beneath the Alaska Peninsula along Alaska-Aleutian subduction zone. *Geophysical Research Letters*, *45*(8), 3453-3460.

Li, D., & Liu, Y. (2016). Spatiotemporal evolution of slow slip events in a nonplanar fault model for northern Cascadia subduction zone. *Journal of Geophysical Research: Solid Earth*, *121*(9), 6828-6845.

Lin, J. T., Aslam, K. S., Thomas, A. M., & Melgar, D. (2020). Overlapping regions of coseismic and transient slow slip on the Hawaiian décollement. *Earth and Planetary Science Letters*, 544, 116353.

Loveless, J. P., & Meade, B. J. (2010). Geodetic imaging of plate motions, slip rates, and partitioning of deformation in Japan. *Journal of Geophysical Research: Solid Earth*, *115*(B2).

Ma, S., & Nie, S. (2019). Dynamic Wedge Failure and Along-Arc Variations of Tsunamigenesis in the Japan Trench Margin. *Geophysical Research Letters*, 46(15), 8782-8790.

Mai, P. M., & Beroza, G. C. (2002). A spatial random field model to characterize complexity in earthquake slip. *Journal of Geophysical Research: Solid Earth*, *107*(B11), ESE-10.

McCaffrey, R., Qamar, A. I., King, R. W., Wells, R., Khazaradze, G., Williams, C. A., ... & Zwick, P. C. (2007). Fault locking, block rotation and crustal deformation in the Pacific Northwest. *Geophysical Journal International*, *169*(3), 1315-1340.

Melgar, D. (2020). dmelgarm/MudPy: v1.2 (Version v1.2). Zenodo. http://doi.org/10.5281/zenodo.3703200

Melgar, D., & Bock, Y. (2015). Kinematic earthquake source inversion and tsunami runup prediction with regional geophysical data. *Journal of Geophysical Research: Solid Earth*, *120*(5), 3324-3349.

Melgar, Diego, and Gavin P. Hayes. "The correlation lengths and hypocentral positions of great earthquakes." *Bulletin of the Seismological Society of America* 109.6 (2019): 2582-2593.

Melgar, Diego, et al. "Kinematic rupture scenarios and synthetic displacement data: An example application to the Cascadia subduction zone." *Journal of Geophysical Research: Solid Earth* 121.9 (2016): 6658-6674.

Melgar, D., Williamson, A. L., & Salazar-Monroy, E. F. (2019). Differences between heterogenous and homogenous slip in regional tsunami hazards modelling. *Geophysical Journal International*, *219*(1), 553-562.

Michel, S., Gualandi, A., & Avouac, J. P. (2019). Interseismic coupling and slow slip events on the Cascadia megathrust. *Pure and Applied Geophysics*, *176*(9), 3867-3891.

Moreno, M., Melnick, D., Rosenau, M., Bolte, J., Klotz, J., Echtler, H., ... & Hase, H. (2011). Heterogeneous plate locking in the South–Central Chile subduction zone:

Building up the next great earthquake. *Earth and Planetary Science Letters*, *305*(3-4), 413-424.

Moreno, M., Rosenau, M., & Oncken, O. (2010). 2010 Maule earthquake slip correlates with pre-seismic locking of Andean subduction zone. *Nature*, *467*(7312), 198-202.

Okada, Y. (1985). Surface deformation due to shear and tensile faults in a half-space. *Bulletin of the seismological society of America*, *75*(4), 1135-1154.

Ozawa, S., Nishimura, T., Suito, H., Kobayashi, T., Tobita, M., & Imakiire, T. (2011). Coseismic and postseismic slip of the 2011 magnitude-9 Tohoku-Oki earthquake. *Nature*, *475*(7356), 373-376.

Ramos, M. D., & Huang, Y. (2019). How the transition region along the Cascadia megathrust influences coseismic behavior: Insights from 2-D dynamic rupture simulations. *Geophysical Research Letters*, *46*(4), 1973-1983.

Ruhl, C. J., Melgar, D., Grapenthin, R., & Allen, R. M. (2017). The value of real-time GNSS to earthquake early warning. *Geophysical Research Letters*, 44(16), 8311-8319.

Ruiz, J. A., Fuentes, M., Riquelme, S., Campos, J. & Cisternas, A. (2016). Numerical simulation of tsunami runup in northern Chile based on nonuniform k−2 slip distributions, *Natural Hazards* 79(2), 1177–1198.

Schmalzle, G. M., McCaffrey, R., & Creager, K. C. (2014). Central Cascadia subduction zone creep. *Geochemistry, Geophysics, Geosystems*, *15*(4), 1515-1532.

Spiess, F. N., Chadwell, C. D., Hildebrand, J. A., Young, L. E., Purcell Jr, G. H., & Dragert, H. (1998). Precise GPS/Acoustic positioning of seafloor reference points for tectonic studies. *Physics of the Earth and Planetary Interiors*, *108*(2), 101-112.

Tozer, B., Sandwell, D. T., Smith, W. H. F., Olson, C., Beale, J. R., & Wessel, P. (2019). Global bathymetry and topography at 15 arc sec: SRTM15+. *Earth and Space Science*, *6*(10), 1847-1864.

Watanabe, S. I., Bock, Y., Melgar, D., & Tadokoro, K. (2018). Tsunami scenarios based on interseismic models along the Nankai trough, Japan, from seafloor and onshore geodesy. *Journal of Geophysical Research: Solid Earth*, *123*(3), 2448-2461.

Wang, K., Wells, R., Mazzotti, S., Hyndman, R. D., & Sagiya, T. (2003). A revised dislocation model of interseismic deformation of the Cascadia subduction zone." *Journal of Geophysical Research: Solid Earth* 108.(B1).

Williamson, A. L., Melgar, D., Crowell, B. W., Arcas, D., Melbourne, T. I., Wei, Y., & Kwong, K. (2020). Toward near-field tsunami forecasting along the Cascadia subduction zone using rapid GNSS source models. *Journal of Geophysical Research: Solid Earth*, e2020JB019636.

Williamson, A., Melgar, D., and Rim, D. (2019). The Effect of Earthquake Kinematics on Tsunami Propagation. *Journal of Geophysical Research: Solid Earth* 124.11: 11639-11650.

Yokota, Y., Ishikawa, T., & Watanabe, S. (2018). Seafloor crustal deformation data along the subduction zones around Japan obtained by GNSS-A observations. *Scientific data* 5: 180182.